IEEE Photonics Journal
An IEEE Photonics Society Publication

Open Access

Broadband Antireflection Subwavelength Structures on Fused Silica Using Lower Temperatures Normal Atmosphere Thermal Dewetted Au Nanopatterns

Volume 8, Number 1, February 2016

Xin Ye
Jin Huang
Feng Geng
Laixi Sun
Hongjie Liu
Xiaodong Jiang
Weidong Wu
Xiaotao Zu
Wanguo Zheng

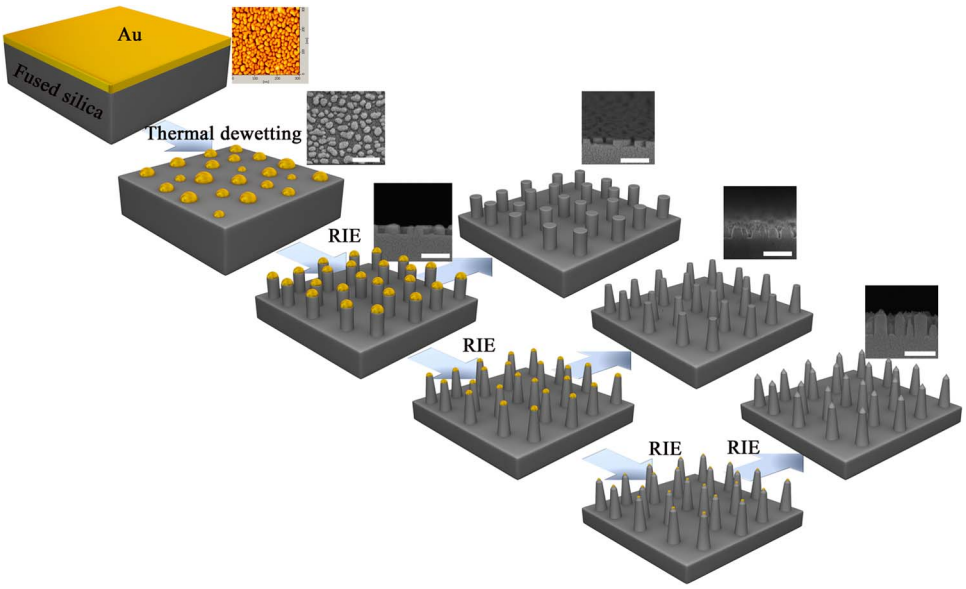

DOI: 10.1109/JPHOT.2015.2508723
1943-0655 © 2015 IEEE

IEEE photonics SOCIETY

IEEE

Broadband Antireflection Subwavelength Structures on Fused Silica Using Lower Temperatures Normal Atmosphere Thermal Dewetted Au Nanopatterns

Xin Ye,[1] Jin Huang,[1] Feng Geng,[1] Laixi Sun,[1] Hongjie Liu,[1] Xiaodong Jiang,[2] Weidong Wu,[2] Xiaotao Zu,[3] and Wanguo Zheng[1,4]

[1]Research Center of Laser Fusion, China Academy of Engineering Physics, Mianyang 621900, China
[2]Science and Technology on Plasma Physics Laboratory, Research Center of Laser Fusion, China Academy of Engineering Physics, Mianyang 621900, China
[3]School of Physical Electronics, University of Electronic Science and Technology of China, Chengdu 610054, China
[4]IFSA Collaborative Innovation Center, Shanghai Jiao Tong University, Shanghai 200240, China

DOI: 10.1109/JPHOT.2015.2508723
1943-0655 © 2015 IEEE. Translations and content mining are permitted for academic research only. Personal use is also permitted, but republication/redistribution requires IEEE permission. See http://www.ieee.org/publications_standards/publications/rights/index.html for more information.

Manuscript received September 30, 2015; revised December 6, 2015; accepted December 8, 2015. Date of publication December 17, 2015; date of current version December 24, 2015. This work was supported in part by the State Key Laboratory of Ultra-Precision Machining Technology Foundation of China Academy of Engineering Physics (CAEP) under Fund ZZ13021 and Fund ZZ14010, by the National Key Scientific Instrument and Equipment Development Project of China under Grant 2014YQ090709, by the National Natural Science Foundation of China under Grant 60908023, and by the Science and Technology Development Foundation of CAEP under Grant 2010B0401055 and Grant 2013A0302016. Corresponding authors: X. Jiang and W. Zheng (e-mail: jiangxdong@ 163.com; yehanwin@mail.ustc.edu.cn).

Abstract: The antireflection (AR) performance and far-field transmittance, depending on the morphology and parameters of subwavelength structures (SWSs), have been investigated by a 3-D finite-difference time-domain (FDTD) method. It is found that far-field transmission characteristics are dominated mainly by period of SWSs. If the period is increased above 220 nm, the far-field transmittance rapidly decreases for a short-wavelength region. An effective and inexpensive method for fabricating disordered SWSs on fused silica has been demonstrated in this paper. An Au nanoscale island mask was formed by lower temperatures thermal dewetted at normal atmosphere. Then, a disordered SWS was fabricated by reactive ion etching (RIE). The average diameter of the Au nanoscale island was easily controlled by the thickness of Au thin films and annealing temperature. The etched depth and shape of fused silica SWSs depend additionally on RIE duration, thus achieving efficient AR characteristics. The measured data and calculated results obtained by the FDTD method exhibit reasonably similar tendencies. The optimized single-side fused silica SWS that is tapered on the tips leads to a significantly high transmissivity value of 96.2%. In addition, it exhibits a broadband AR property at a wavelength range of 400–1100 nm.

Index Terms: Subwavelength structures, low-temperature thermal dewetting, effective medium theory, finite-difference time domains, optical properties.

1. Introduction

Anti-reflection (AR) technology is currently used across a myriad of different applications [1], [2], such as light-emitting diodes [3], flat-panel displays, solar cells [4], and optical sensors [5]. The

decrease in transmission of a transparent optical medium is mainly caused by the abrupt change in the refractive index at the interface between a medium and its environment [6]. If the refractive index of medium for light propagation does not abrupt change or the refractive of different media are same, this light reflection will be suppressed to near zero. Over the past few decades, thin film coatings which have gradient or intermediate refractive indices are commonly utilized to reduce surface reflective loss [1], [2]. However, the multilayered thin film has problems associated with limitations in the coating materials and various physical and chemical properties. Those problems will affect the stability of the film coatings stack because of adhesion and thermal mismatch [7]. Recently, a subwavelength structured (SWS) surface was utilized to suppress the surface reflection of media. The surface relief structure has a dimension smaller than the wavelength of incidence light [8]–[11]. For the subwavelength structure layer on the substrate, the effective refractive index of SWS is determined by the fraction of the air and the structural materials at the direction of incident light. Therefore, the refractive index of the SWS can be continuous and monotonous change from boundary of air/SWS to that of SWS/substrate, when the morphology of SWS is idea cone profile [6]. The SWS surface has distinct advantages compared to films [12]. First, the material of the SWS is the same as that of substrate, but film materials with appropriate refractive index are rare in nature. Second, the SWS exhibit higher physics and chemical properties durability than films because the materials of SWS and substrate are same, and the SWS has robust mechanical stability due to etching in substrate [13]. Finally, the SWS have more tunable parameters than thin film, such as the cross-sectional geometry, height, and spacing [14].

Numerical solution of Maxwell's equations has been used to accurately study the optical performance of SWS. Even through the SWS has been analysis by the rigorous coupled wave analysis (RCWA) [3] and finite-difference time-domain (FDTD) [15] method, previous works have focused on total reflectance or total transmittance of SWS. The change of far field transmittance spectrum (0th diffraction) depending on the modulation of the SWS morphology has not been reported actively. The total transmittance consists of high order diffraction and far field transmittance, and low reflectivity does not necessarily correspond to high far field transmittance because of high order diffraction of periodicity SWS or scattering of random SWS. In this work, the antireflection performance and far field transmittance depending on the morphology and parameters of nanopillar arrays, such as height, period and spacing of nanopillars, have been investigated by 3-D-FDTD method.

In the last decade, the increasing effort about fabrication of such surface antireflection structures has been devoted. Many researchers reported various effective creation of high performance antireflection periodic SWS by several method, including electron-beam lithography [16], laser interference lithography [17], microsphere monolayer colloidal crystals [18], [19] and nanoimprint lithography [20] for nanoscale etch mask patterns. The antireflection performance of silicon SWS have been widely studied, but few works devoted to the transparent surface antireflection, such as fused silica and quartz. The optical properties of the transparent material are different from those of semiconductors which have inherent light absorption properties. Fused silica is widely applied for optical and optoelectronic field, such as display, optical lens, and high-power laser field [21].

Recently, the interests in antireflection structures have been extended to random structures. Two-dimensional metal nanoscale thin films which were deposited on dielectric substrates are typically thermodynamically unstable. The nanoscale thin film become statistical nanostructures as the result of dewetting after heated. The statistical nanostructures were prepared on a substrate. Then it can be acted as a shadow mask during the subsequent SWS fabrication. The method will be relatively efficient, simple, and inexpensive, compared to the fabrication of periodic SWS. Therefore, it is particularly applicable for large areas application [22]–[24]. However, this method still has critical drawbacks for wide application. The sophisticated equipment and vacuum technology are requirement for thermal dewetting such as rapid thermal annealing (RTA) system. Additionally, high temperatures and rapid thermal annealing for the thermal dewetting process can lead to the residual stress of optical elements. It will limit the widely application of optical elements. However, there have been few works on the fabrication of SWS on fused silica using lower temperature thermal dewetted Au nanoparticles by muffle furnace at normal atmosphere.

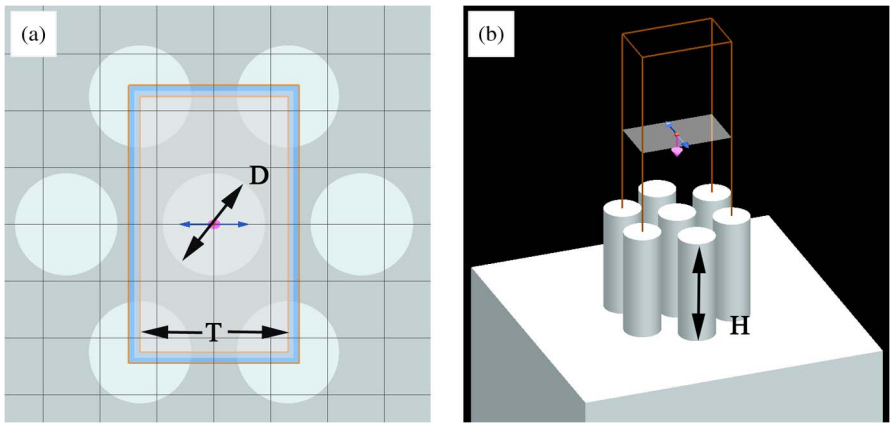

Fig. 1. Unit cell of numerical calculation was designed in rectangle lattices $(T * \sqrt{3}\ T)$, where T is period of unit cell, D is diameter of nanopillar, and H is height of nanopillar. (a) Top view of the calculations model. (b) Tilted-view of the calculations model. Note that the arrow is the incident direction of light and that the blue arrow is the polarization direction.

In this paper, we improve the thermal annealing etching-mask technique and report a simple and effective method for creating SWS by using lower temperatures at normal atmosphere thermal annealing statistical nanoscale islands upon a fused silica substrate. The size of statistical nanoscale islands can be adjusted by the muffle furnace annealing temperature and the thick of Au films. The antireflective characteristics of disordered fused silica SWS was fabricated by reactive ion etching (RIE) process. In this process, the thermally dewetted Au nanoscale islands acted as shadow masks. The innovative AR technology based on SWS has been shown to have great potential for increasing the reliability, decreasing the fabrication cost and larger scale application.

2. Numerical Calculations

To better understanding the optical performance of SWS, the finite-difference time domain (FDTD) method was used to calculate Maxwell's equations. Therefore, it is valid for all texture size-to-wavelength ratios, including long and short wavelength limits. In our case, the SWS is a 3-D random structure. It appears to be a difficult task to model. Even though the SWS fabricated using dewetted Au nanopatterns do not have periodic structure, it is noteworthy to analyze the reflectance by the variation of the period of SWS to determine the optimal distance of each pillar of SWS. This is because the size of structure is smaller than light wavelength. Therefore we have adopted a simplified approach by using the 3-D Six-fold hexagonal symmetric nanostructures with pillar shapes. The incidence light was set plane waves. As the diffraction efficiency of the periodic structure is very low polarization dependent for 2-D structure. The polarization direction was set as shown in Fig. 1(b) (blue arrow). And periodic boundary conditions were set around a unit cell, while perfectly matched layer (PML) absorbing boundary conditions were used at the top and bottom boundaries of the cell. In the following, we consider surfaces coated by a periodic pillar texture with height H, Diameter D, and period T. The unit cell was designed in rectangle lattices$(T * \sqrt{3})$, as shown in Fig. 1. The fill factor f_{silica} of nanopillar was set $\pi D^2/2\sqrt{3}T^2$. The spacing of pillar arrays was (T-D).

Fig. 2(a) shows the color map of the calculated total reflectance of pillar arrays as a function of diameter of nanopillar (50 to 280 nm) and wavelength (300 to 1100 nm) at normal incidence. The period T was set 280 nm. And the height H was set 220 nm. It is observed that fused silica substrate with 220 nm diameter nanostructures exhibits a minimum reflectance of below 0.5% at normal incidence. Therefore, the optimal fill factor of nanopillar should be 0.56 for high performance antireflection. In the case, the spacing of nanopillar arrays should be 60 nm. From Fig. 2(b), we can see that the color map of the variation of calculated total transmittance results variation as a

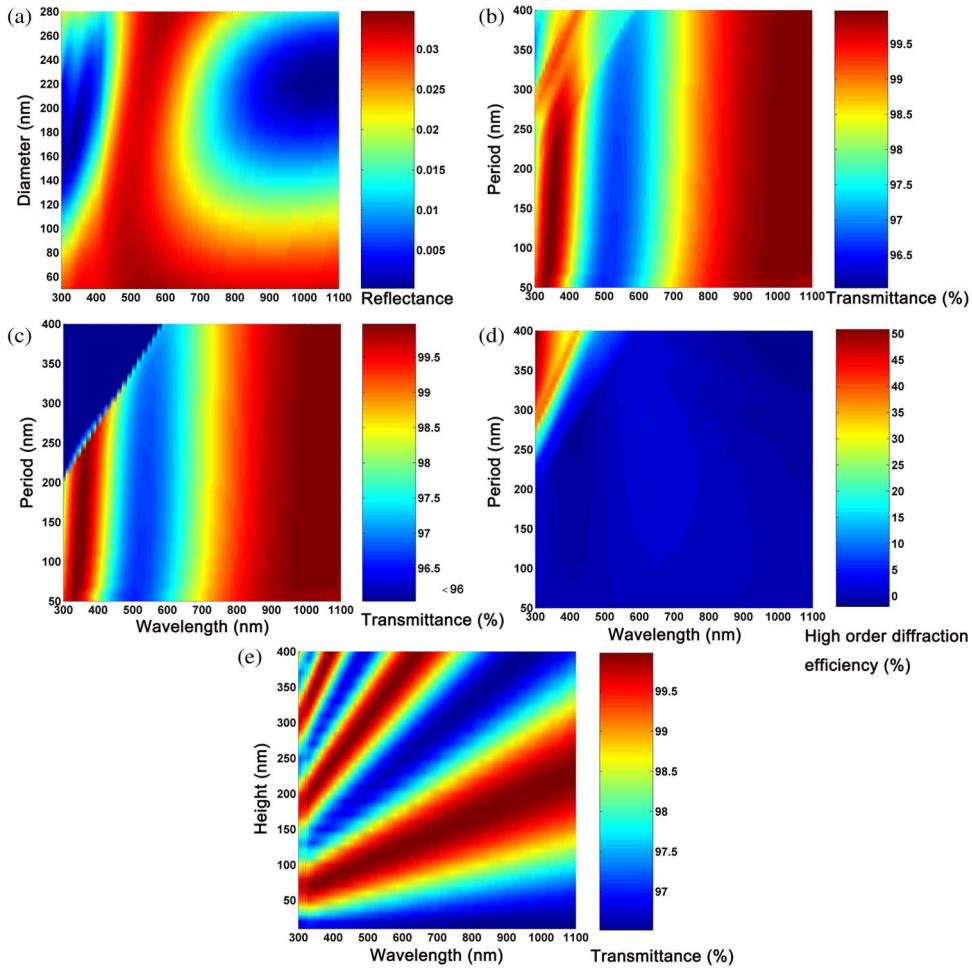

Fig. 2. Two-dimensional contour plots of the calculated antireflection performance. (a) Calculated reflectance for the various diameters of nanopillar. (b) Total transmittance for the various period of unit cell. (c) Far field transmittance for the various period of unit cell. (d) High order diffraction efficiency for the various period of unit cell. (e) Far field transmittance for various height of nanopillars.

function of wavelength for period in the unit cell with 220 nm in height and 0.56 in fill factor. The average total transmittance of the surface structured pillar arrays is above 99.5% for the design placed on fused silica substrate from 800 nm to 1100.

Fresnel reflection of an incident light is an electromagnetic phenomenon which comes from different reflective index as a consequence of the sudden change of the reflective index at an interface of two materials. A simple method of suppressing Fresnel reflection at an optical interface is insert a single layer with a matching refractive index which broken the sudden change of refractive index in to smaller steps. The lower reflection was obtained. Actually, the nanopillar layer can acts as an effective medium (n_{eff}) that approximates a single layer coating, therefore, the total transmittance of the nanopillar layer is greatly like that of a single layer antireflection thin film.

From simply effective medium theory (EMT), the SWS on fused silica substrate can act as an inserted single layer. The effective refractive index can be approximated by $n_{\text{eff}} = [f_{\text{silica}} \cdot n_{\text{silica}}^q + (1 - f_{\text{silica}}) \cdot n_{\text{air}}^q]^{1/q}$, where $q = 2/3$, where f_{silica} is the silica filling factor, $n_{\text{air}} = 1$, and $n_{\text{silica}} = 1.46$ are the refractive index of air and fused silica substrate, respectively [6]. The effective refraction index is apparently determined by the silica filling factor and refractive index of the substrate. To achieve small reflectance, the effective reflective index is equal to the square root of the substrate refractive index, where the incident medium is air with 1 in refractive index. The height of pillar, H,

is 1 quarter wave in optical thickness, $H = \lambda/4n_{eff}$, where λ is the wavelength at which the transmittance maximum is to occur.

However, higher far field transmittance is very important for antireflection performance application, and low reflectivity does not necessarily correspond to high field transmittance because of high order diffraction of periodicity SWS or scattering of random SWS. Fig. 2(c) shows far field transmittance of the SWS fused silica as a function of wavelength and for period in the unit cell with 220 nm in height, 0.58 in fill factor of pillar. We can see when the period of the unit cell is decreased below 220 nm, the far field transmittance spectrum similar to total transmittance spectrum. It means that there is not high order diffraction efficiency from 300 nm to 1100 nm. If the period is increased above 220 nm, the far field transmittance decreases rapidly for short wavelength region. The far field transmittance decreases for larger periods while high diffraction orders begin to emerge. That is because the features move out of the subwavelength regime for the shorter wavelengths. For better understanding of the mechanism of high order diffraction, we reveal the high order diffraction efficiency for wavelengths in relation to the various periods of the SWS in Fig. 2(d). The high order diffraction efficiency increases monotonous as the period of SWS increases. Fig. 2(e) shows far field transmittance of the SWG fused silica as a function of wavelength and height of nanopillar. As the height is increased from 0 to 400 nm, there are more fluctuations in far field transmittance as the height increases due to the interference of light reflected at the top and bottom of the SWS layer at each wavelength.

3. Experimental Details

The fused silica substrates were polished (roughness value below 1 nm), soaked in the mixture of 98% H_2SO_4/30% H_2O_2 (volumetric ratio 3 : 1) for 30 min under boiling (with ultrasonic wave), and then rinsed with deionized water (18.2 MΩ cm^{-1}) several times and dried with N_2 stream. The size of the fused silica substrate is 20 mm $*$ 20 mm $*$ 1 mm. All chemicals (analytical grade) were supplied by Aldrich and used without further purification.

An Au film was then evaporated on the fused silica substrate surface using a thermal evaporating system. To obtain the disorder Au nanoscale islands as an etching-mask, the samples were annealed using muffle furnace under the atmosphere. Muffle furnace at different temperatures of 150 °C, 200 °C, and 300 °C and the temperature rise is 40 °C/min, and the annealing time was kept at 30 min then natural cooling. During the thermal dewetting process, the Au thin films are agglomerated into the nanoscale islands due to their increased surface energy of the Au film by the heating.

Using the Au nanoscale island patterns, the nanopillar SWS surfaces were fabricated on fused silica substrates by an RIE process in fluorine radical plasma. The RIE process was performed using He (150 sccm) and CHF_3 (15 sccm) at RF power 100 w, chamber pressure 10 pa, for appropriate time. Finally, the residual Au material was removed by chloroazotic acid solution (the mixture of 37% HCl and 70% HNO_3, volumetric ratio 3 : 1).

The morphology of Au thin film was analyzed using a MFP-3D-SA AFM (Asylum research). The morphology of the Au nanoscale islands and the fused silica SWS were analyzed using a FEI FESEM Nova450 scanning electron microscope with an accelerating voltage of 5.0 kV. The samples were sputtered with a thin layer of Pt prior to imaging. The transmittance spectra of the structured and unstructured samples were measured with a UV-VIS-NIR spectrophotometer (PerkinElmer Lambda950) in the wavelength range of 300 to 1100 nm.

4. Results and Discussion

The fabrication process of SWS surfaces used in this study is shown in Fig. 3. First, an Au nano-film was deposited on the fused silica substrate by thermal evaporation. The AFM of Au thin film morphology was indicated by the wave line. Second, the samples are then heated at appropriate temperature for 30 min in muffle furnace to induce thermal dewetting of deposited Au film. Then, the fused silica with the Au nanoscale islands was etched by a CHF3 reactive ion etching (RIE) process. As the etching rate of Au is much lower than that of fused silica under

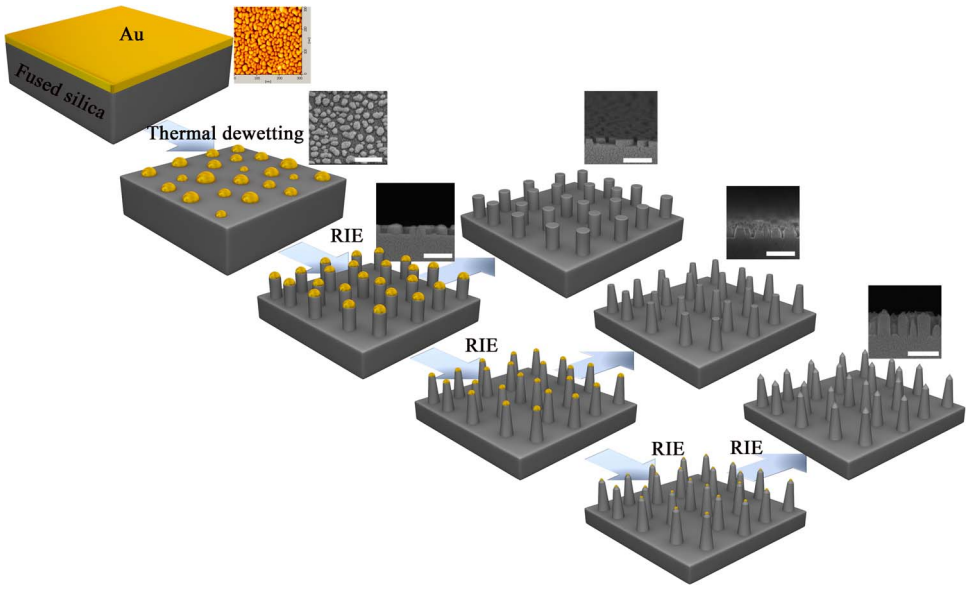

Fig. 3. Schematic illustration of the process steps for fabricating SWS on fused silica (scale bar 500 nm).

above RIE conditions, the Au nanoscale island protect fused silica immediately underneath them from being etched, resulting in the formation of nanopillar directly on fused silica surface. In the process of RIE, the Au nanoscale islands are masks, but they can also be etched by the reactive ions. In the beginning, the fused silica pillar-link structures are formed after removing the Au masks. The size of the Au nanoscale islands reduces during the etching, which leads to formation of truncated taper-shaped profile after removing the masks. After the Au nano-islands are removed by reactive ions completely, the fused silica pillar-like structures with taper tops are obtained. Etching times of 8 min–25 min were used to generate fused silica SWS with different heights. Finally, once the fused silica pillars are deep enough, the Au nanoscale island at the tips of pillars can be selectively removed by etching with aqua regia solution. The shapes and density of the SWS are also well consistent with those of original Au nanoscale islands.

We can control the average diameter of Au nanoscale islands and spacing between the nearest Au nanoscale islands by the Au film thickness and the annealing temperature. Fig. 4 shows a scanning electron microscope (SEM) image presenting the evolution of nanoscale island morphology on fused silica surface over a range of thicknesses and temperatures for an annealing of 30 min. The film thicknesses of 3 nm and 5 nm are represented in rows. And columns display the samples processed at annealing temperatures at 150 °C, 200 °C, and 300 °C, respectively. The morphology of nanoscale islands, such as diameter and spacing of nearest island depend strongly on the thickness of Au films and the annealing temperature. Agglomeration proceeds occur as the heating temperature increases, since the high annealing temperature enhances the surface energy of nanometer thin film on the surface of substrate. As shown in Fig. 4(a)–(c), a transition from interconnected networks to bicontinuous-spinodal pattern and then separated individual droplets occurred for the thicker Au films (5 nm) with increasing the annealing temperature. From Fig. 4(c), we can see that the Au nanoscale film is completely separated into hemispherical nanoisland profile with nanoscale size at the 300 °C.

However, when the thickness of film is thinner, such as 3 nm, the surface morphologies variation transition is shown in a different manner. When the sampled was annealed at 150 °C, as shown in Fig. 4(d), the Au film is separated hemispherical individual nanoscale island, while the nanoscale islands have minor diameter and short distance between islands. Longer spacing between islands and fewer nanoscale islands in the same area are found as the annealing temperature

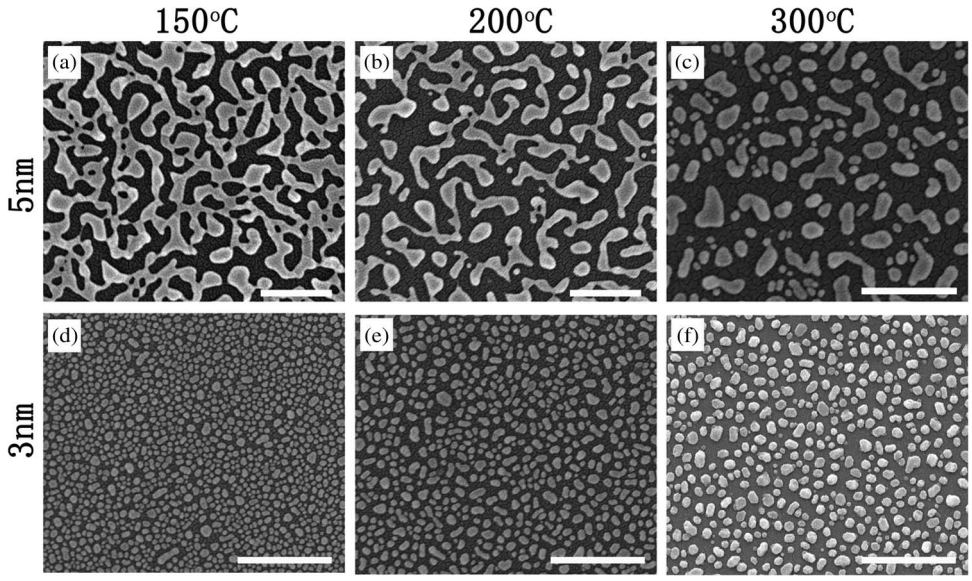

Fig. 4. SEM micrographs displaying the evolution of film morphology of Au thin films of 3 and 5 nm annealed at 150–300 °C for 30 min. (scale bar 500 nm).

increases. In the meantime, the nanoscale islands become increasingly large the average diameter (see Fig. 4(e) and (f)). On the other hand, the size of the Au nano-islands and the distance between nanoscale islands are increased at the same annealing temperature with the thickness of Au films is increased. (Fig. 4, each column) Low annealing temperature lead to large and bicontinuous shapes, which are not adequate for fused silica SWS mask patterns. On the other hand, the thinner Au films cannot act as a etch mask due to a mask erosion effect arising from the high density of energetic ions in the plasma. Under these considerations, the 5 nm thickness of Au film and 300 °C temperature of annealing, which are enough to make SWS with period less than 200 nm and height larger than 300 nm, was chosen for the fabrication of SWS integrated ultraviolet and visible light applications. It is revealed that the etch mask was composed of high-density randomly arranged nanoscale islands with various shapes. These islands are non-closely packed on the fused silica surface. Under the present experiment conditions, the dimensions of the Au islands range from 40 to 200 nm. Because heating rate of muffle furnace is low, and the heating-up time is long, the surface nanopattern can be controlled by the temperatures and thickness of thin film. The thinner Au thin film is required at a low annealing temperature and normal atmosphere, such as the thickness should be less than 10 nm.

To get the value of f_{silica} we used image processing methods in MATLAB software to calculate the number of nanoscale islands and to verify the mean size of the Au islands. The dimensions of the Au islands highly range from 120 nm to 160 nm. Therefore, we decided to use 5 nm thickness Au films at 300 °C annealing temperature for further etching process (see Fig. 2(c)).

To investigate the shape transition process of the Au nanoscale island masks and the obtained structures underneath, the etching time was set for 8 min to 25 min in our experimental process. The average height of fused silica SWS increases from 90 nm to 330 nm as the etching duration increased from 8 min to 25 min. After 8 min etching, fused silica pillar-like structures with about 90 nm in height were formed on the surface of fused silica substrate (see Fig. 5(a)). And the tops of pillar arrays were smooth. The SEM images of fused silica SWS after 15 min etching is shown in Fig. 5(b). Au nanoscale island masks were etched away gradually as the increase of the etching duration, while the profile of structure transformed from pillar-like to frustum of taper. The height of structure is 223 nm and the tops of them were rough. As shown in Fig. 5(c), the Au nanoscale islands which acted as masks obviously change into nanodots profile with the increase of the etching duration and finally vanish after etching of 25 min. The fused

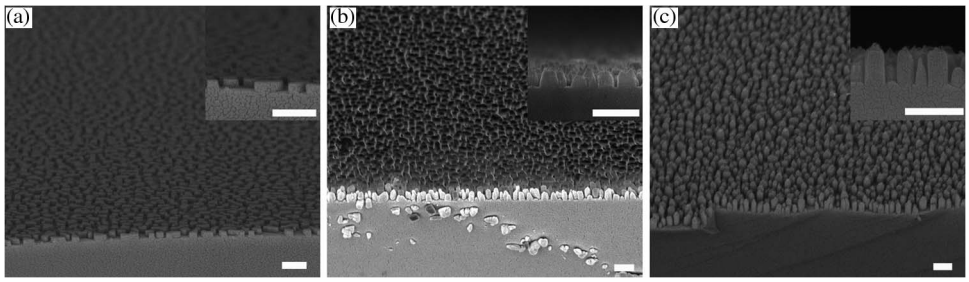

Fig. 5. SEM photographs of SWS on fused silica obtained by detuning the RIE duration at (a) 8, (b) 15, and (c) 25 min. (Insets) Cross-sectional view SEM images of the corresponding structures. (scale bar 500 nm).

silica SWS change into pillar-like structures with taper top 330 nm in height. The etching rate of fused silica in our case ranges 11 to 13 nm/s.

For better understanding the relation between morphologies and etched duration, the study of the morphologies of the SWS with different RIE time was investigated as fellow. The Au nanoscale islands act as masks, but they also can be etched by the reactive ions during the RIE process. In the beginning, the pillar-link profile (see Fig. 5(a)) is formed on the fused silica surface after 8 min etching. During the etching, the surface of islands becomes rough owing to the etching during RIE process. As shown in Fig. 5(b), the truncated taper-shaped profile formed on the fused silica surface after 15 min etched. This is because the size of the nanoscale islands acted as mask reduces during the etching. In this case, the Au nanoscale islands are completely removed after 25 min etching. In Fig. 5(c), the fused silica pillar-like structures with taper tops are obtained after the Au nanoscale islands mask are removed by reactive ions completely. Therefore, we have prepared fused silica SWS with different morphologies by changing the experimental conditions: from pillar-like, truncated taper shaped to pillar-like arrays with taper top profile.

To investigate the optical properties of the fused silica SWS, Fig. 6(a) shows the transmission spectra of the single side SWS at normal incidence. The fused silica SWS samples showed remarkable antireflective performance from 300 nm to 1100 nm wavelength. For instance, all of the SWS samples which was etched for 8 min, 15 min and 25 min exhibited better optical performances of above 96% at different wavelength region. For SWS etched 8 min, the antireflection wavelength is from 425 nm to 575 nm, and for sample etched 15 min and 25 min, the optimal transmittance wavelength region is 600 nm–875 nm, and 650 nm–1100 nm, respectively. Remarkably, the transmission spectra shown in Fig. 6(a) reveal that the maximum value of specific wavelengths is related to the etching time. This is because the height of the SWS increased as the increase of the etch duration. The transmittance of single side SWS increases significantly (> 96%) at wavelengths of 300 nm~1100 nm, and the fluctuation of the transmittance also changes like a single AR layer. These phenomena have been reported in the single layer antireflective films. Fig. 6(b) shows the corresponding reflection spectra as a function of the incident wavelength, ranging from 300 nm to 1100 nm. In our case, the minimum reflectance for the SWS with 90 nm height occurred less than 500 nm wavelength, and for the SWS with 223 nm and 330 nm height, the incident wavelength where the minimum reflectance occurred were around 650 nm and 1000 nm, respectively. The minimum reflectance of single side SWS for the 90 nm, 223 nm, and 330 nm height was almost the same, approaching 3.5–4%. The experimental reflectance measurements are complemented by theoretical calculations using a 3D-FDTD method. As shown in Fig. 6(b) and (d), the simulated spectra agree reasonably well with the optical measurements for single-side SWS on fused silica substrate at lone wavelength region. The reflectance spectra cannot agree well with the simulation result in the short wavelength region. This is because the SWS in our case have taper-shaped profile, and they exhibit a broadband antireflection property.

To investigate the scattering of fused silica SWS, the sum of the transmittance and reflectance of the SWS was expressed in Fig. 6(c). All the samples with SWS on the surface have a

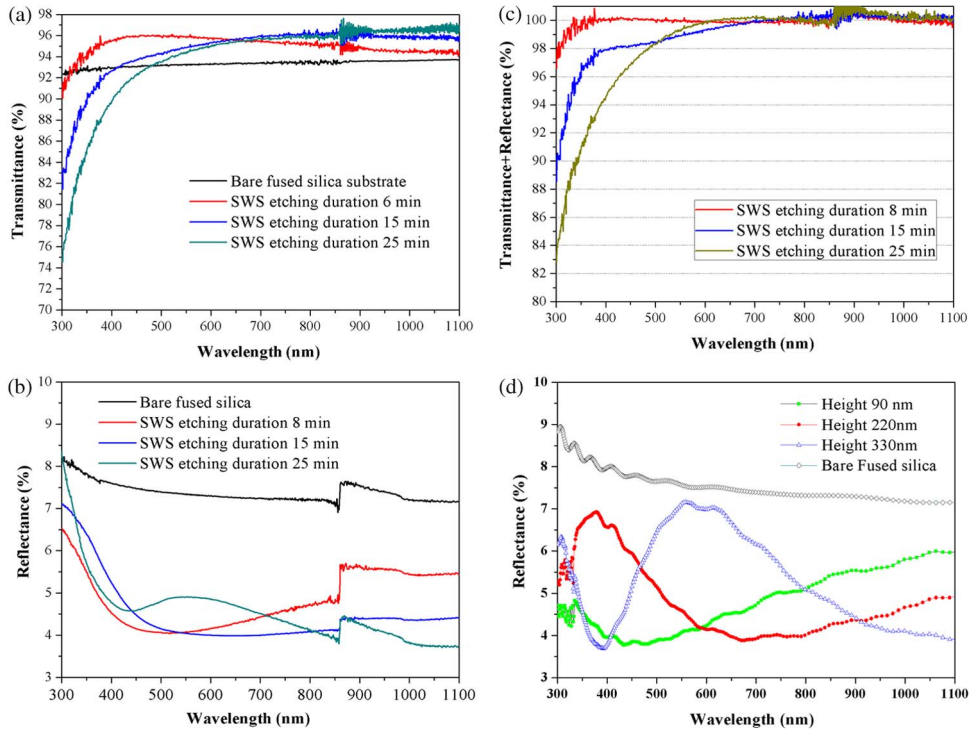

Fig. 6. (a) Measured transmittance spectra, (b) total reflectance, and (c) transmittance plus total reflectance of the fabricated single side SWS etched for 8, 15, and 25 min using thermally dewetted Au nanoparticles after annealing of 300 °C for 5 nm Au film. Note the detector change at about 860 nm. (d) Simulated optical reflectance at normal incidence.

sum of transmittance and reflectance less than 1. The result shows that the light loss often is at the short wavelength region, which we will discuss as follows. Previously, some researchers have reported similar phenomenon. The sum of transmittance and reflectance of the SWS surface is lower than bare substrate in the short wavelength region [25]. The deficiency in the short wavelength was attributed to the scattering on the SWS. The scattering on the fused SWS is probably resulted from Rayleigh scattering [26], and the Rayleigh scattering is valid for sizes when structure meet the formula $d \ll \lambda/(\pi n_{\text{silica}})$, where λ is the optical wavelength and the height and the size of the SWS may be acted as the sizes of structure d. The sum of transmittance and reflection will decrease for SWS on fused silica substrate because the light scattering increases as the height of fused silica SWS increases.

For ideal SWS with broadband antireflective, the effective refractive index n_{eff} should gradually increase from 1 to n_{silica} from the air to that of fused silica substrate. And this requires the tapered shapes of the SWS, from the effective reflective index n_{eff} equation. As revealed by the Fig. 5(b), formation of truncated taper-shaped profile obtained at 15 min etching time have tapered sidewalls, which results in gradual change n_{eff} in the fused silica SWS layer so that its broadband antireflective wavelength range is from 600 nm–875 nm (see Fig. 6(a) blue). Further extending the etching duration can result in the pillar-like structures with taper top (see Fig. 3(c)); therefore, the 25-min etched sample exhibits broadband reflective from 650 nm–1100 nm (see Fig. 6(a) dark cyan).

5. Conclusion

The far field transmittance and high order diffraction efficiency spectra as a function of period of SWS was investigated using 3-D-FDTD method. We can see that the far field transmittance spectrum similar to total transmittance spectrum, when the period of SWS is smaller than 220 nm. It means that there is not high order diffraction efficiency from 300 nm to 1100 nm. The antireflection

SWS on the fused silica substrate were fabricated by lower temperatures thermal dewetted Au nano-island mask based on muffle furnace at normal atmosphere and then RIE in fluorine-base plasma. It is easily possible to control the average diameter of the Au nanoscale islands in order to optimize the optical properties by the thickness of thin films and low-cost annealing technology. The thinner thickness of the thin Au films (< 10 nm) and long anneal time are need to insure fabrication of nano-island mask by low temperatures anneal technology. It is found that the fabricated fused silica SWS exhibited high performance broadband antireflective properties from 400 nm to 1100 nm wavelength range.

References

[1] L. Martinu and D. Poitras, "Plasma deposition of optical films and coatings: A review," *J. Vac. Sci. Technol. A*, vol. 18, no. 6, pp. 2619–2645, Nov./Dec. 2000.

[2] X. Ye *et al.*, "Subwavelength porous silica antireflection coating," *J. Optoelectron. Adv. Mater.*, vol. 13, no. 5, pp. 532–536, May/Jun. 2011.

[3] Y. C. Kim and Y. R. Do, "Nanohole-templated organic light-emitting diodes fabricated using laser-interfering lithography: Moth-eye lighting," *Opt. Exp.*, vol. 13, no. 5, pp. 1598–1603, Mar. 2005.

[4] Y. M. Song, J. S. Yu, and Y. T. Lee, "Antireflective submicrometer gratings on thin-film silicon solar cells for light-absorption enhancement," *Opt. Lett.*, vol. 35, no. 3, pp. 276–278, Feb. 2010.

[5] D. S. Hobbs, B. D. MacLeod, and J. R. Riccobono, "Update on the development of high performance anti-reflecting surface relief micro-structures," in *Proc. SPIE Conf. Window Dome Technol. Mater. X*, Orlando, FL, USA, 2007, vol. 6545, pp. 1–14.

[6] H. A. Macleod, *Thin-Film Optical Filters*, 3rd ed. Boca Raton, FL, USA: CRC, 2001.

[7] J. Q. Xi *et al.*, "Optical thin-film materials with low refractive index for broadband elimination of Fresnel reflection," *Nat. Photon.*, vol. 1, no. 3, pp. 176–179, Mar. 2007.

[8] P. B. Clapham and M. C. Hutley, "Reduction of lens reflection by moth eye principle," *Nature*, vol. 244, no. 5414, pp. 281–282, Aug. 1973.

[9] W. H. Miller, G. D. Bernard, and J. L. Allen, "Optics of insect compound eyes—Microcomponents with dimensions near a wavelength of light cause observable optical effects," *Science*, vol. 162, no. 3855, pp. 760–767, Nov. 1968.

[10] X. Ye *et al.*, "Broadband antireflection and self-cleaning random grass structure on silicon," *J. Optoelectron. Adv. Mater.*, vol. 17, no. 1, pp. 192–197, Jan./Feb. 2015.

[11] X. Ye *et al.*, "Formation of broadband antireflective and superhydrophilic subwavelength structures on fused silica using one-step self-masking reactive ion etching," *Sci. Rep.*, vol. 5, 2015, Art. ID 13023.

[12] H. Kikuta, H. Toyota, and W. Yu, "Optical elements with subwavelength structured surfaces," *Opt. Rev.*, vol. 10, no. 2, pp. 63–73, Mar. 2003.

[13] Y. Du *et al.*, "Laser-induced damage properties of subwavelength antireflective grating on fused silica," *Thin Solid Films*, vol. 567, pp. 47–53, Sep. 2014.

[14] Y. M. Song, H. J. Choi, J. S. Yu, and Y. T. Lee, "Design of highly transparent glasses with broadband antireflective subwavelength structures," *Opt. Exp.*, vol. 18, no. 12, pp. 13063–13071, Jun. 2010.

[15] C. Lee, S. Y. Bae, S. Mobasser, and H. Manohara, "A novel silicon nanotips antireflection surface for the micro sun sensor," *Nano Lett.*, vol. 5, no. 12, pp. 2438–2442, Dec. 2005.

[16] Y. Kanamori, M. Sasaki, and K. Hane, "Broadband antireflection gratings fabricated upon silicon substrates," *Opt. Lett.*, vol. 24, no. 20, pp. 1422–1424, Oct. 1999.

[17] P. Y. Baroni *et al.*, "Nanostructured surface fabricated by laser interference lithography to attenuate the reflectivity of microlens arrays," *J. Eur. Opt. Soc.-Rapid Publ.*, vol. 5, Jan. 2010, Art. ID 10006.

[18] Y. H. Tang, M. J. Huang, J. Y. Su, and M. H. Shiao, "Fabrication of nanocone subwavelength antireflection structures on quartz substrates," *Jpn. J. Appl. Phys.*, vol. 51, no. 6S, Jun. 2012, Art. ID 06FF06.

[19] X. Ye *et al.*, "Subwavelength structures for high power laser antireflection application on fused silica by one-step reactive ion etching," *Opt. Lasers Eng.*, vol. 78, pp. 48–54, Mar. 2016.

[20] T. Yanagishita, T. Endo, K. Nishio, and H. Masuda, "Preparation of antireflection SiO_2 structures based on nanoimprinting using anodic porous alumina molds," *Jpn. J. Appl. Phys.*, vol. 49, no. 6R, Jun. 2010, Art. ID 065202.

[21] H. J. Liu *et al.*, "Subsurface defects characterization and laser damage performance of fused silica optics during HF-etched process," *Opt. Mater.*, vol. 36, no. 5, pp. 855–860, Mar. 2014.

[22] G. C. Park, Y. M. Song, E. K. Kang, and Y. T. Lee, "Size-dependent optical behavior of disordered nanostructures on glass substrates," *Appl. Opt.*, vol. 51, no. 24, pp. 5890–5896, Aug. 2012.

[23] M. Sakhuja *et al.*, "Omnidirectional study of nanostructured glass packaging for solar modules," *Progr. Photovolt.*, vol. 22, no. 3, pp. 356–361, Mar. 2014.

[24] D. Infante *et al.*, "Durable, superhydrophobic, antireflection, and low haze glass surfaces using scalable metal dewetting nanostructuring," *Nano Res.*, vol. 6, no. 6, pp. 429–440, Jun. 2013.

[25] F. L. Gonzalez, D. E. Morse, and M. J. Gordon, "Importance of diffuse scattering phenomena in moth-eye arrays for broadband infrared applications," *Opt. Lett.*, vol. 39, no. 1, pp. 13–16, Jan. 2014.

[26] O. L. Muskens, J. G. Rivas, R. E. Algra, E. Bakkers, and A. Lagendijk, "Design of light scattering in nanowire materials for photovoltaic applications," *Nano Lett.*, vol. 8, no. 9, pp. 2638–2642, Sep. 2008.